Synchrotron X-ray radioscopic in situ study of high-temperature polymer electrolyte fuel cells — Effect of operation conditions on structure of membrane

Tobias Arlt [a],[*], Wiebke Maier [b], Christian Tötzke [a], Christoph Wannek [b], Henning Markötter [a], Frank Wieder [a], John Banhart [a], Werner Lehnert [c], Ingo Manke [a]

[a] Helmholtz-Zentrum Berlin GmbH, Institute of Applied Materials, Hahn-Meitner-Platz 1, 14109 Berlin, Germany
[b] Forschungszentrum Jülich GmbH, Institute of Energy and Climate Research, IEK-3: Electrochemical Process Engineering, 52425 Jülich, Germany
[c] Modeling in Electrochemical Process Engineering, RWTH Aachen University, Germany

HIGHLIGHTS

- High temperature PEM fuel cells were investigated with synchrotron radiography.
- First in-operando analysis of distribution of phosphoric acid in the MEA was performed.
- Significant changes in media distribution possibly caused by varying degree of acid.
- Strong movements of electrode fragments were found and analyzed quantitatively.

ARTICLE INFO

ABSTRACT

We present the first high-resolution synchrotron X-ray study on high temperature polymer electrolyte fuel cells (HT-PEFCs) in through-plane mode. Distribution and evolution of the phosphoric acid in the membrane electrode assembly was monitored in situ/in-operando under different operating conditions at steady states. At current densities of 350 mA cm^{-2} and 600 mA cm^{-2} significant changes in local media distribution were detected mainly beneath the channels of the flow field. We assign this effect to a varying degree of acid doping over the active region. Furthermore it was found that parts of the electrode structure were moved and partly irreversibly displaced after cell operation at load conditions. This effect might contribute to structural aging of the electrodes.

© 2013 Elsevier B.V. All rights reserved.

1. Introduction

In recent years, much research was carried out to optimize the water management of low-temperature fuel cells [1,2]. Non-destructive methods such as neutron or synchrotron X-ray imaging sometimes complemented by additional in situ techniques, e.g. current density measurements, were successfully applied to study the influence of the water distribution on the performance of low temperature fuel cells [3–19]. In contrast the water management of high-temperature fuel cells (HT-PEFCs) is directly linked to the

equilibrium state of the phosphoric acid derivatives. However, adequate in situ studies on variations in concentration and distribution of phosphoric acid are still rare [20–22]. Synchrotron imaging offers high spatial and temporal resolution and allows for in situ analyses of dynamic transport processes. Compared to laboratory X-ray sources synchrotron sources provide enhanced beam intensity and quality and the opportunity to use monochromatic radiation [23,24]. For these reasons, synchrotron imaging is the most suitable approach for small-scale and non-destructive investigations of fuel cells and has, for instance, already been successfully applied to observe aging effects in DMFCs [16,25].

In contrast to low-temperature polymer electrolyte membrane (PEM) fuel cells, HT-PEFCs feature high carbon monoxide (CO)

* Corresponding author. Tel.: +49 30 8062 42822; fax: +49 30 8062 43059.
E-mail address: tobias.arlt@helmholtz-berlin.de (T. Arlt).

tolerance and can therefore be operated with low-purity gas (such as reformat gas). Furthermore gas humidification is not required (although possible and sometimes beneficial [26,27]) since the proton conduction mechanisms differ from those in low temperature fuel cells. The proton conduction mechanisms within HT-PEFCs proceed by different reactions. These mechanisms are the Grotthus mechanism [28] and the $PBI-H_3PO_4-H_2O$ conduction mechanism [29]. Thereby phosphoric acid reacts with water produced in the reactions and thereby forms equilibrium with the acids dehydration products (mainly pyro-phosphoric acid $H_4P_2O_7$) [30,31]. In the following, this water is referred to as 'product water'. Product water can also dilute the phosphoric. At operating temperatures around 160 °C one primarily expects two derivatives of phosphoric acid that occur in HT-PEFCs: ortho-phosphoric acid (H_3PO_4) and pyro-phosphoric acid ($H_4P_2O_7$). Since hydration and dehydration of phosphoric acid results in a changing X-ray attenuation coefficient, the composition of phosphoric acid can be investigated in situ by means of transmittance synchrotron X-ray imaging. This information is hardly accessible by any other measurement method due to the acidic environment present in HT-PEFCs.

In this study, HT-PEFCs were analyzed in situ by means of synchrotron X-ray radioscopy. A dedicated test cell design was used in order to achieve high beam transmittance through the cell for both the through-plane (perpendicular to membrane layer) and in-plane (in parallel to membrane layer) perspectives. In addition to previous results [20] we achieved highly resolved spatial information about the distribution of phosphoric acid inside the membrane electrode assembly (MEA) in through-plane.

2. Experimental

2.1. Imaging setup

Radiography was performed with the tomography station at the BAM*line* (electron storage ring BESSY II of the Helmholtz-Zentrum Berlin) [32]. The synchrotron beam was monochromatized to 22 keV using a double multilayer monochromator with an energy resolution of about $\Delta E/E = 1.5\%$ [33]. The detector system comprised a 20-μm thick $CdWO_4$ scintillator, a microscopic optic and a pco4000 camera [34] with a 4008×2672 pixel^2 CCD chip that is kept out of the direct beam by using a mirror (see Fig. 1). With the

settings chosen, each detector pixel corresponded to a sample area of 2.15×2.15 μm^2, while the temporal resolution was 8 s (6.5 s exposure time and 1.5 s read out time).

2.2. Fuel cells and MEA preparation

The cell design was specially developed for radiographic measurements by Forschungszentrum Jülich. The flow field was adapted in order to enhance beam intensity in the in-plane and through-plane orientations by drilling through-holes into the end plates thereby reducing the material thickness of the flow field plates. A single channel serpentine flow field geometry was used at the anode and cathode sides, as shown in Fig. 2. The channel depth was 2.5 mm; the widths of the channel and the rib were 1.5 mm. The active region was 49 cm^2 large.

Two identical cells were investigated in this study, referred to as HTT1 and HTT2 in the following. Prior to radiography, HTT1 was subjected to a break-in procedure at the Forschungszentrum Jülich, meaning that it was operated at a current density of $j = 200$ mA cm^{-2} for 70 h in a test rig. Subsequently, it was shut down and transferred into a mobile test rig in order to perform radiography and impedance spectroscopy at BESSY II. No such break-in procedure was performed for test cell HTT2. This cell was assembled on-site just 2 h prior to radiography.

A commercially available gas diffusion layer (GDL) composed of non-woven carbon fibers with a micro porous layer on one side (H2315 C2, Freudenberg FCCT KG) was coated with a dispersion of carbon-supported catalyst (20% HP Pt on Vulcan XC-72, BASF Fuel Cell, Inc.), PTFE (Dyneon, 40 wt% in the final catalyst layer) and dispersants applying the doctor blade technique. The gas diffusion electrodes (GDEs) were produced with a platinum loading of ∼1 mg cm^{-2}. After drying at room temperature, the anodic and the cathodic catalyst layers were each doped with 20 mg cm^{-2} phosphoric acid using a solution of ethanol:85% aqueous phosphoric acid (4:1 w/w). This solution was pipetted dropwise as a quadratic grid over the whole electrode area until the final doping level had been reached (see also Ref. [35]). After this, the GDEs were joined with a 30-μm thick undoped poly(2,5-benzimidazole) (ABPBI) membrane (FuMA-Tech GmbH) in a test cell without preceding hot-pressing.

The cells were heated up stepwise at ambient pressure to approach the operating temperature of 160 °C, see Fig. 3. For all the
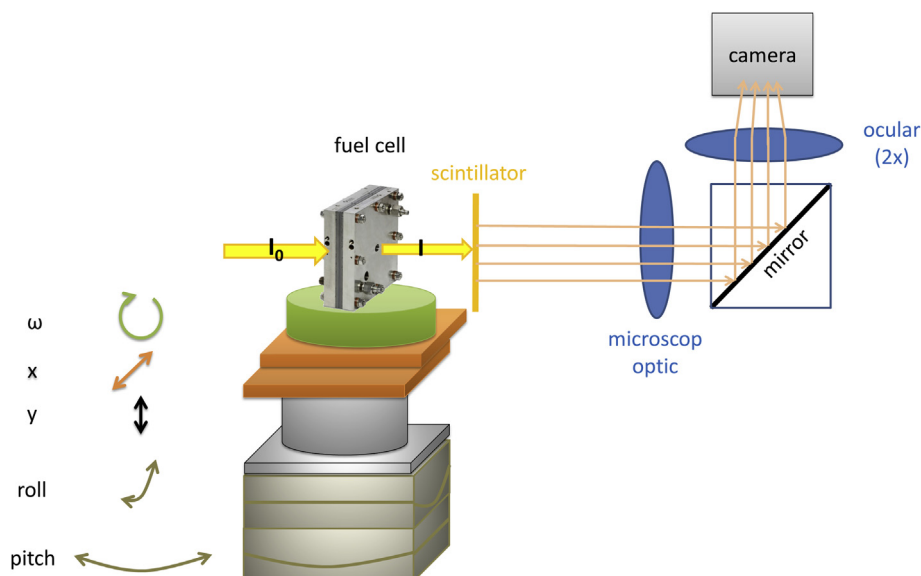

Fig. 1. Experimental setup of the tomography station at BAM*line* (Helmholtz–Zentrum Berlin, Germany).
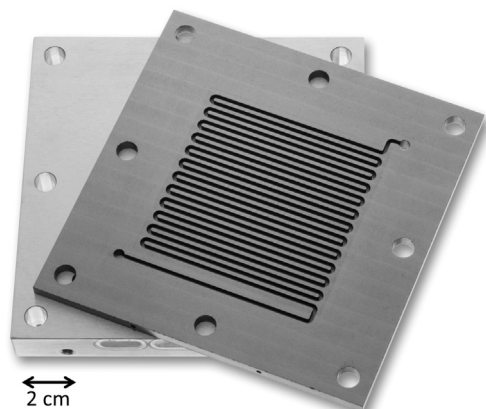
Fig. 2. Meandering single channel gas flow field geometry was used at the anode and cathode sides.

Fig. 4. Through-plane perspective of center part of cell HTT1 (flat- and darkfield-corrected radiographs). Flow field channels show up as bright areas, whereas the ribs appear dark. The anodic and cathodic flow field patterns show a slight vertical mismatch (for descriptions please see text above).

experiments, dry gases were supplied and the flow rates of hydrogen and air at current densities equal to or greater than $j = 140$ mA cm^{-2} were adjusted to meet the stoichiometric rates of $\lambda_{An/Ca} = 2/2$ or 4/4, respectively. At open circuit voltage (OCV) the flow rates were kept equivalent to $\lambda_{An/Ca} = 2/2$ at $j = 140$ mA cm^{-2} for the duration of 2 h. After the operation at OCV the cells were operated at increasing current densities (140 mA cm^{-2}, 350 mA cm^{-2} and 600 mA cm^{-2}) at stoichiometric rates of $\lambda_{An/Ca} = 2/2$ and $\lambda_{An/Ca} = 4/4$, see Fig. 3. The current densities were kept constant for 40 min to achieve steady state conditions inside the MEA. After this, the cells were operated under OCV for 2 h again. Radiographs were continuously taken throughout the entire experiment.

3. Results

Through-plane radiographs were taken from the center of the active region where all the channels are parallel to each other and are arranged horizontally, as shown in Fig. 2. The dominating features of cell HTT1 as shown in Fig. 4 are the regular channel-rib pattern of the flow fields and the irregular pattern of cracks within the catalyst layers which originates from a fabrication step of the electrodes. The anodic and cathodic flow fields are aligned with only little overlap, visible by the double structure of the
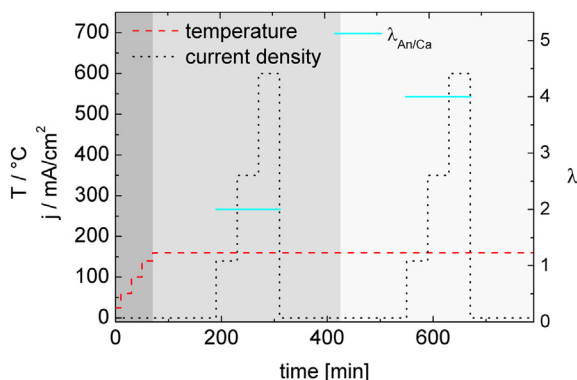

Fig. 3. Sketch of the measuring procedure which shows three parts. Dark gray rectangle represents the heating up, following by two almost identical programs (first program was run with a stoichiometry of $\lambda_{An/Ca} = 2/2$ while $\lambda_{An/Ca} = 4/4$ was used for second program) which are marked by gray and light gray rectangles respectively. Both programs were run starting at open circuit voltage (OCV) for 2 h, followed by operating conditions at different current densities for about 40 min.
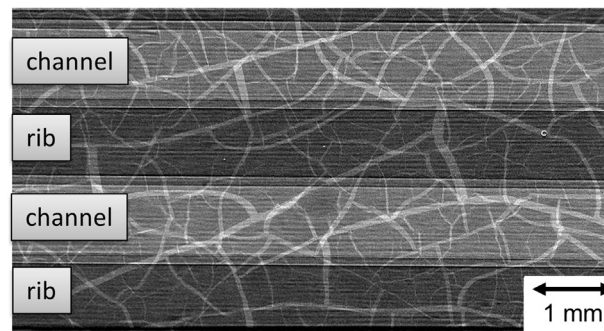
channel edges. The reason for the overlap (107 μm for cell HTT1 and 12 μm for cell HTT2) is a mismatch of anode sided and cathode sided flow field in the projection which occurred during cell construction. Since the mismatch is small compared to the flow field dimension this does not affect the operation significantly. The electrodes have a fragmented appearance on both the anode and the cathode side. The cracks in the electrodes are narrower underneath the ribs compared to those underneath channel areas. This is caused by the compressing of the cell which also compresses the fragments of the electrodes.

The series of normalized images in Fig. 5 represents the changes in transmittance of cell HTT1 (for the same image section as shown in Fig. 4) at different current densities but at constant stoichiometries $\lambda_{An/Ca} = 2/2$. The radiographs were normalized with respect to a radiograph taken after OCV had been applied for 2 h. Light gray values (>1) indicate an increase of transmittance under load conditions while darker values (<1) indicate lower transmittance. At a current density of 140 mA cm^{-2} (Fig. 5a) no significant change of transmittance was detectable. Upon increasing the current density to 350 mA cm^{-2} (Fig. 5b) local changes of the transmittance showed up and intensified after the current density had further been increased to 600 mA cm^{-2} (Fig. 5c). The images in Fig. 5 reveal a change (increase and decrease) in the local transmittance of up to 1% especially beneath the channel areas (see Fig. 5c). These changes can be assigned either to a changed distribution of the liquid media or alternatively to inhomogeneous swelling of the membrane (see below). Furthermore, bright white stripes at the edges of the electrode fragments become visible. They are caused by movement of the electrode fragments or by changes of their shapes. These two different kinds of transmittance changes will be separately investigated.

Changes within channel areas are more pronounced than those of rib areas. Note that the scale of transmittance variation during the measurement is small (a few tenths of a percent). In order to visualize the differences, strong contrast enhancement was performed in Figs. 5–7, which, however, also gave rise to artifacts such as horizontal streaks and bright spots which are produced by the monochromator and scintillator defects.

The dimension of individual areas affected by a positive or negative change in transmittance in Fig. 5 is in the same range as the width of the channels and broader than maximum electrode fragments dimensions. These areas form an almost periodical pattern with a period of around 1 mm. Furthermore the sharp transmittance changes at the electrode fragment edges seem to be somehow correlated to this periodical structure, i.e. they appear mainly in areas with strong overall changes in the transmittance. In some cases a correlation between the individual shape of an
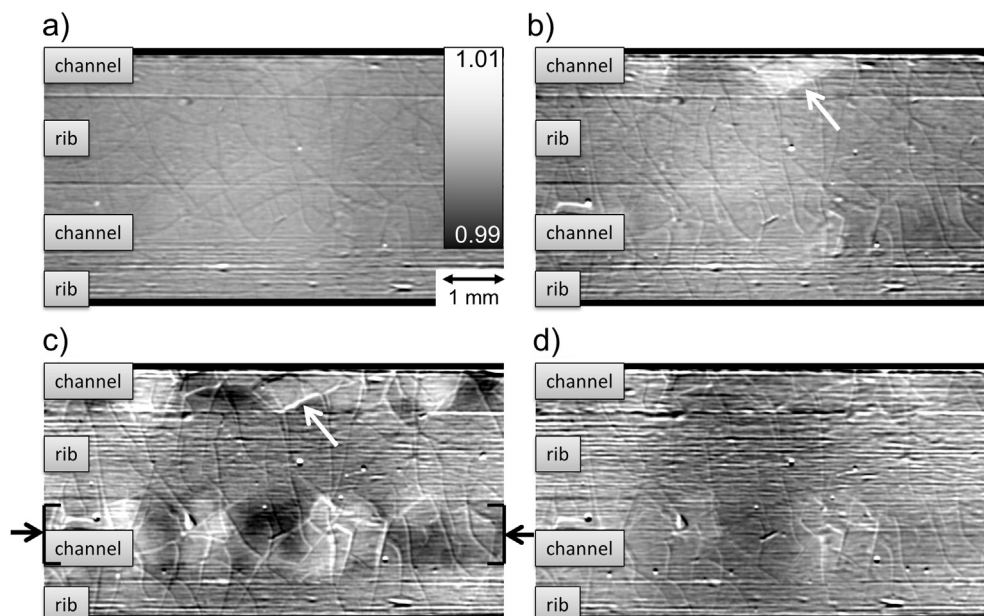
Fig. 5. Cell HTT1 operated at different current densities (1-fold serpentine flow field, 160 °C, $\lambda = 2/2$) normalized to the operation condition after 2 h at OCV. a) 140 mA cm^{-2}, b) 350 mA cm^{-2}, c) 600 mA cm^{-2}, d) 0 mA cm^{-2} (OCV). In order to achieve steady state conditions, only radiographs taken at the end of each operating condition were chosen. Gray values show the changes of normalized transmittances between 0.99 (black) and 1.01 (white). The region shown is the same as in Fig. 4. The area between the black markers in c) was taken for line plot which are shown in Fig. 8b–d.

electrode fragment and that of the zone with altered transmittance can be found. This is quite obvious at the top of Fig. 5b and c (marked by white arrows) where the outer edges of fragments perfectly match with the borders of areas with a changed transmittance.

It is interesting to remark that the overall periodic structure remains unchanged for different operating conditions as exemplarily shown in Fig. 6b and c (indicated by white circles). Furthermore the structure is reproducible after restart of the cell. Locations of maxima and minima of the structures in Figs. 5c and 6c are almost identical (note: Radiographs in Figs. 5 and 6 are taken from the same location in the cell, see above). The electrode fragments change their locations by a few microns (see white arrow in Fig. 6c and d). Fig. 5d indicates that after about 2 h of cell operation at OCV local transmittance changes are still present. Apparently, the operation at non-zero current densities induced irreversible changes of the cell structure.

In a further experiment the current density was again increased in discrete steps, this time at increased stoichiometry of $\lambda_{An/Ca} = 4/4$. Fig. 6 shows the resulting changes of the transmittances which are less pronounced than those observed at lower stoichiometries.

Fig. 7 shows the development in cell HTT2 during the stepwise increase of current density at a stoichiometry of $\lambda_{An/Ca} = 2/2$. Changes of transmittance and fragment movements are very similar to those observed for cell HTT1 at $\lambda_{An/Ca} = 2/2$. Again, the local changes of transmittance and the dislocation of fragments are most pronounced beneath the channel regions. Overall, the fragment displacement appears to be stronger in cell HTT2 than in cell HTT1. Especially in regions of large transmittance changes, fragment displacements are not totally restored. Some of these locations are marked by white arrows in Fig. 7c and d.

For a better comparison of the transmittance changes in the fuel cell during operation at different conditions, profiles were calculated along horizontal lines through the radiographs in Figs. 5–7. The position of two of such lines is marked in Figs. 5c and 8a. The line plots have a width of 1 mm (i.e. all transmittance values have been averaged over 1 mm width) and were taken from the channel

area over the whole width of the radiographs. Fig. 8b–d shows sets of line plots for cell HTT1 and HTT2. Each line plot corresponds to a given operating condition defined by the respective stoichiometry and current density.

4. Discussion

Due to the different attenuation coefficients of ortho- and pyrophosphoric acid the hydration by product water during the fuel cell reaction or the dehydration at OCV of the acid implies a significant change on the overall transmittance.

To analyze the possible reasons for the local changes in transmittance observed during the measurements variations of material thickness and phosphoric acid composition must be taken into account. Local transmittance changes can be caused by different effects:

1. Chemical changes, e.g. $H_3PO_4 \rightarrow H_4P_2O_7$ and vice versa,
2. Filling of empty pores with H_3PO_4, $H_4P_2O_7$ or ABPBI.

Table 1 summarizes the scenarios of material conversion and redistribution that could account for relative transmittance changes in the range of $-0.8\% \leq \Delta T \leq 0.7\%$. This interval was chosen with respect to the detected transmittance variations given in Fig. 8. This includes hydration and dehydration of phosphoric acid, membrane swelling as well as subsequent warping of the membrane. The thicknesses were calculated using

$$d(T_{\text{load}}, \mu_1, \mu_2) = \ln\frac{T_{\text{load}}}{T_{\text{OCV}}}/(\mu_2 - \mu_1) \tag{1}$$

which is a variant of the Beer–Lambert's law under the simplifying assumption that all other conditions remain constant. Here, $d(T_{\text{load}}, \mu_1, \mu_2)$ denotes the thickness of the transmitted layer in which the present material with attenuation coefficient μ_1 was "converted" into another material with attenuation coefficient μ_2. $T_{\text{load}}/T_{\text{OCV}}$ is the change of relative transmittance. Changes of material thickness
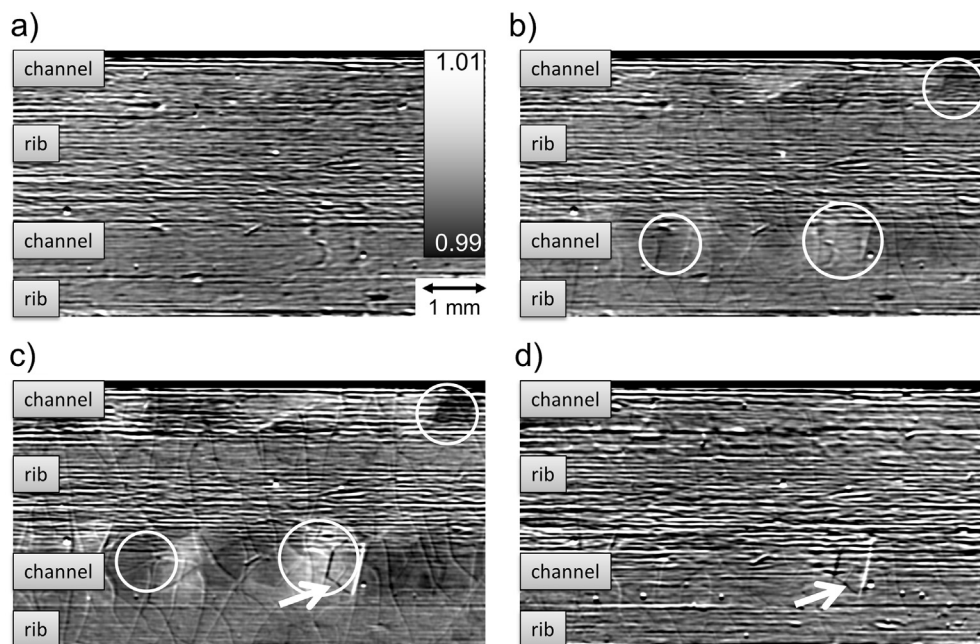
Fig. 6. Cell HTT1 operated at different current densities (1-fold serpentine flow field, 160 °C, $\lambda = 4/4$) normalized to the operating condition after 2 h at OCV. a) 140 mA cm^{-2}, b) 350 mA cm^{-2}, c) 600 mA cm^{-2}, d) 0 mA cm^{-2} (OCV). Gray values show the changes of normalized transmittances between 0.99 (black) and 1.01 (white). The region shown is the same as in Fig. 4.

can be induced by replacing, redistributing (adding or removing of material in the field of view, which lead to locally changed transmittances) or swelling. The calculation was performed for different assumed materials in the MEA. Table 1 includes coefficient differences between various phosphoric acid derivatives and membrane material as well as H$_2$, O$_2$, steam or air in "empty" pores inside the MEA components. The thickness $d_{\Delta T = x}$ (x stands for a change of transmittance in percent) refers to the thickness of transmitted

material that is affected by the assumed material changes in order to achieve a transmittance changes of $\Delta T = x$.

As an example we consider a relative transmittance change of -0.5% which is a typical value measured for HTT1 at 600 mA cm^{-2}. If this change was exclusively generated by the substitution of H$_3$PO$_4$ for H$_4$P$_2$O$_7$ the corresponding thickness of the converted material layer would be 127 μm. Taking into account the initial MEA thickness at OCV and the amount of phosphoric acid added into the
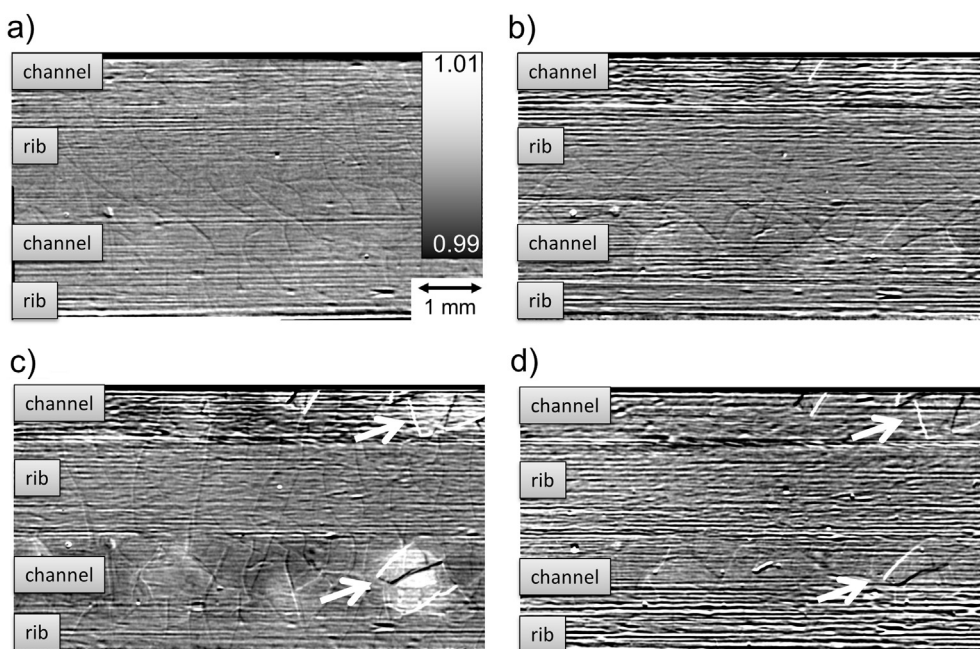

Fig. 7. Cell HTT2 operated at different current densities (1-fold serpentine flow field, 160 °C, $\lambda = 2/2$) normalized to the operating condition after 2 h at OCV. a) 140 mA cm^{-2}, b) 350 mA cm^{-2}, c) 600 mA cm^{-2}, d) 0 mA cm^{-2} (OCV). Gray values show the changes of normalized transmittances between 0.99 (black) and 1.01 (white). Irreversible fragment movements are observable, indicated by white arrows. The presented region is comparable to that shown in Fig. 4.
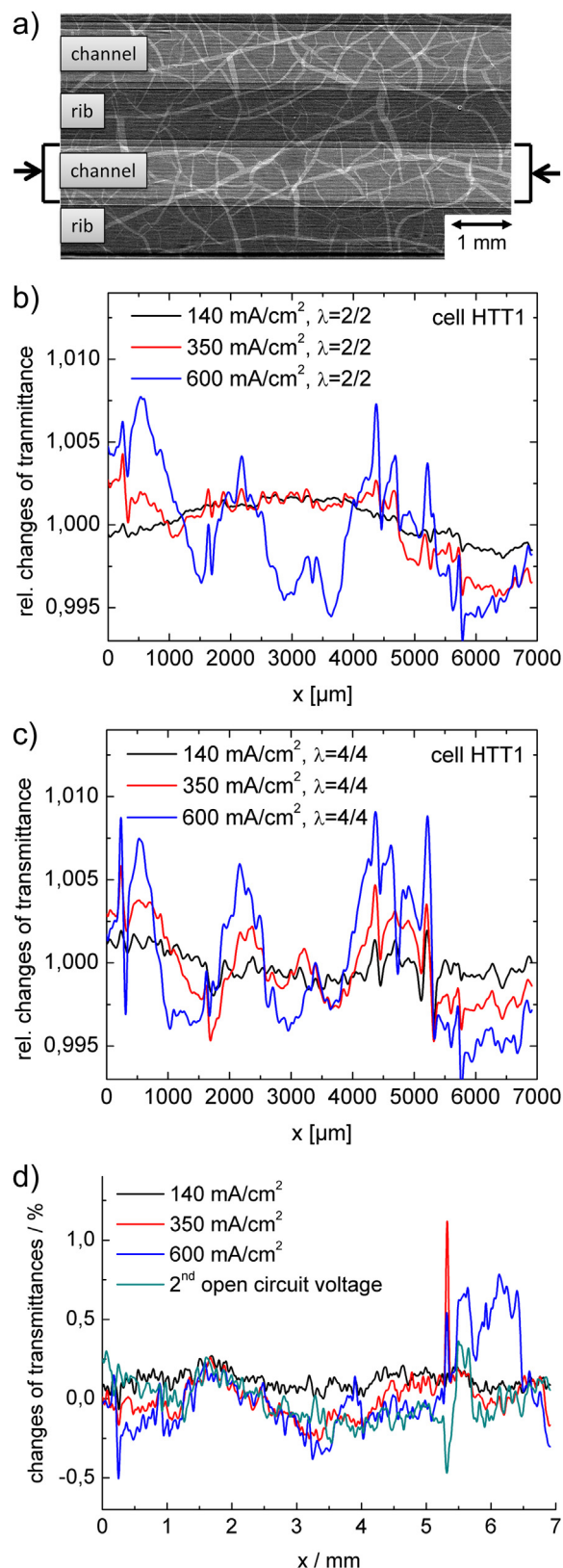
Fig. 8. a) Normalized radiograph taken at OCV condition and $\lambda_{An/Ca} = 4/4$. The plots were obtained by averaging transversal along the path represented by the black markers as the path was congruent with the lower channel. This was performed in Figs. 5–7. b) Cell HTT1 (with break-in procedure) for a stoichiometry of $\lambda = 2/2$ and c) $\lambda = 4/4$ and d) cell HTT2 (without break-in procedure). Pronounced peaks originate from displacement of fragments.

MEA (as described in Section 2.2) this value appears unrealistically high. More likely, the chemical conversion of phosphoric acid is accompanied by a redistribution of the acid derivatives. While acid is pressed into other membrane regions pores are filled or depleted. This causes a warp and a tilt of the fragments which are attached to the membrane. Both, filling of pores and tilting of the membrane into the viewing direction, contribute to an increased projected material thickness and a higher attenuation (e.g. as calculated in lines 3–5 of Table 1 in case of pore filling). Fig. 9 demonstrates the influence of a varying material thickness produced by membrane swelling and by the conversion of phosphoric acid. Since the beam attenuation by gaseous phases is negligible small (<0.01%) the filling of empty pores with acid derivatives or membrane materials results in stronger changes of the transmittance as compared to the sole conversion of acid derivatives.

With respect to the magnitude of measured changes it is reasonable to assume a combination of superposed material redistributions to be responsible for local transmittance variations. A clear distinction of the individual effects is, however, not possible, because measurements in through-plane perspective only yield an overall transmittance signal across MEA and GDLs.

Images in Figs. 5 and 6 and the line plots presented in Fig. 8 show that changes of local transmittances are more pronounced in cell HTT1 which was subjected to a break-in procedure. In freshly assembled fuel cells the phosphoric acid spreads within the MEA components during the break-in procedure due to evolving product water. One possible explanation for the found periodical material redistributions can be the hygroscopic properties of the phosphoric acid. Up to now, there are no investigations on HT-PEFCs concerning the impact of water agglomerations on the distribution of phosphoric acid. Due to locally changing properties of the MEA such as membrane thickness, cell compression or fluctuating doping with phosphoric acid, we assume locally changing properties for HT-PEFCs, too, implying varying impact of the hygroscopic properties. Thus, water vapor is influenced by phosphoric acid agglomerations. The hygroscopic nature of phosphoric acid causes water vapor to move to acid-rich regions due to diffusion or to be produced directly at the three-phase boundary, resulting in a decreased acid mass density [36]. One possibility is the transport of water and acid through the membrane due to the hygroscopic nature of phosphoric acid. At lower viscosity the acid molecules have a higher mobility which facilitates acid rearrangements and, therefore, a more pronounced inhomogeneity of local acid distribution. Theoretically, upon changing to OCV conditions no water is produced at the electrode. As a result, water slowly diffuses out of the membrane and acid concentration and local distribution equilibrates nearly back to the initial conditions. This explains the reversibility and local nature of this effect (Figs. 5–7). The authors assume that the phosphoric acid doping technique is responsible for the fixed location of transmittance changes (i.e. the periodic structure).

However we would like to propose also an alternative explanation for the observed phenomena. The current in the electrode active layers is not uniformly distributed. It is higher in the areas with lower resistance, which are also non-uniformly distributed due to porous electrode structure and non-uniform electrolyte distribution. In the regions with higher currents water is produced more intensively. This water dilutes the acid thus increasing its conductivity and mobility, which results in flooding of neighboring pores by the electrolyte and formation of transport paths for phosphoric acid with higher conductivity and higher current density. As a result the transmittance in the radiographs decreases where the amount of phosphoric acid is increased, while the transmittance increases where the amount of phosphoric acid is decreased (see Fig. 9). The hygroscopic property of the acid forces

Table 1
Attenuation coefficients and differences of attenuation coefficient between various phosphoric acid derivatives and membrane material. Thickness $d_{\Delta T=x}$ (x stands for change of transmittance, rounded to integer μm) refers to the thickness that is necessary to achieve changes in the transmittance by replacing acid volumes or filling pores in the MEA in beam direction and can be obtained using eq. (1). Negative values mean that initially filled pores are emptied. "−" means that the changes in transmittance cannot be caused by the corresponding effect (different algebraic signs).

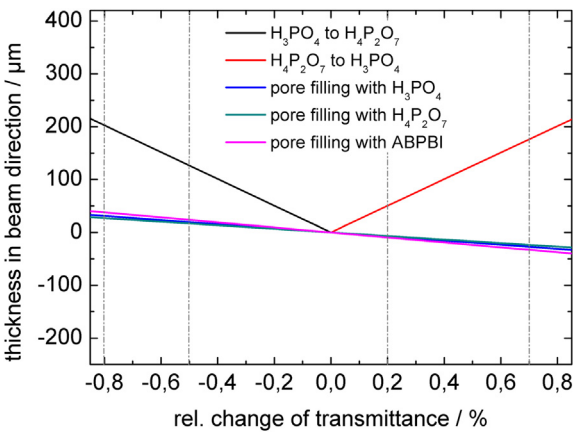|	$\mu_2 - \mu_1$/mm^{-1}	$d_{\Delta T=-0.8\%}$/μm	$d_{\Delta T=-0.5\%}$/μm	$d_{\Delta T=0.2\%}$/μm	$d_{\Delta T=0.7\%}$/μm
$H_3PO_4 \rightarrow H_4P_2O_7$	−0.0396	203	127	−	−
$H_4P_2O_7 \rightarrow H_3PO_4$	0.0396	−	−	50	176
Pores → H_3PO_4	0.2571	31	19	−8	−27
Pores → $H_4P_2O_7$	0.2967	27	17	−7	−24
Pores → ABPBI	0.2120	38	24	−9	−33

Fig. 9. Correlation of change in relative transmittance and material thickness in beam direction. Dotted lines mark the transmittances used for calculations in Table 1.

transport paths absorb nearby acid drops, which results in pore depletion and formation of areas with higher and lower transmittance. As the effect of changing transmittance was observed to be reversible, we assume existing paths to persist for further transports of phosphoric acid. This effect also explains the less pronounced effects in cell HTT2, which was not suspended to a break-in procedure before. Consequently, pores and transport paths for the phosphoric acid through the membrane have to be established during the first cell operation (i.e. during the break-in procedure). Since cell HTT1 was operated before the radiographic measurements, corresponding transport paths inside the membrane have already been created, resulting in more pronounced redistributions due to better transport possibilities.

In the next part we will have a closer look on the variations of transmittance values at the edges of some electrode fragments (see Fig. 6c and d and at the right top of Fig. 7c and d), indicating displacement with respect to their initial position in the reference OCV condition. Since the respective fragments are all situated within areas of significant transmittance change, it is reasonable to assign fragment displacement to local deformation of the MEA. Especially for cell HTT2, some of the fragment displacements are obviously
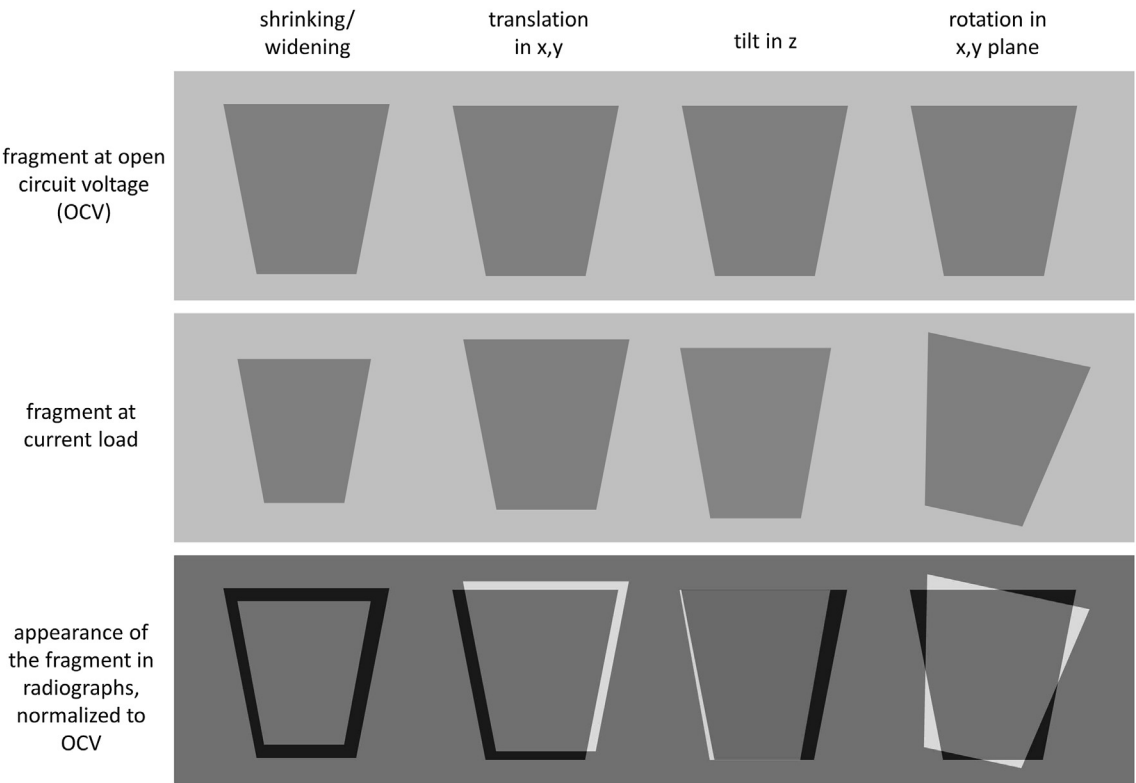

Fig. 10. Possibilities of fragment variances and the corresponding appearance in the normalized radiographs: shrinking/widening, translation, tilting or rotation.

irreversible, see Fig. 7d. Therefore, material redistributions induced by load changes are assumed to modify the fragmented structure of the electrode permanently. Fig. 10 illustrates different possible fragment movements and their corresponding appearance in the normalized radiographs. Also combinations of the effects are possible.

The found bright areas at the edges of the electrode fragments could not only be caused by shrinking/expanding or horizontal movement of the individual electrode fragments, but also by tilting of the fragments that is caused by a local swelling of the membrane (see Fig. 10, third column). Fig. 11a explains the relation between the fragment dimensions L_{frag} and the width a of the bright area at the edge of a fragment. Size of most fragments ranges from 50 to 500 μm diameter. Fig. 11b shows the dependence of fragment dimensions and the edge displacement a on the lift height of fragment edges z (see Fig. 11a). The graphs were computed using the geometrical considerations given in eq. (2).

$$z = L_{fragment} \cdot \sin\left(\arccos\frac{L_{fragment} - a}{L_{fragment}}\right) \qquad (2)$$

The gray areas in Fig. 11b include all combinations of fragment dimensions and tilt displacements found in the normalized radiographs. Frequently measured combinations are highlighted in dark gray indicating that most variances of the fragment position in the z-direction are in the range of 20–60 μm. The magnitude of these values is in line with the calculated changes of material thickness necessary to induce the observed variation of local transmittance and it is also of the same order of magnitude as the total thickness of the MEA (appr. 100 μm) which can be seen as a lower physical limit (minimum membrane 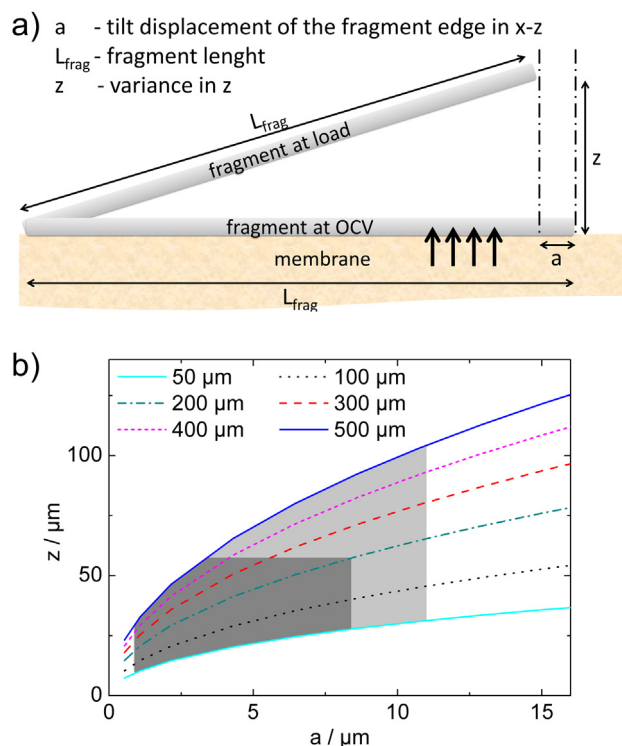thickness is achieved at maximum loss of phosphoric acid to adjacent membrane regions) and upper physical limit (maximum membrane thickness with completely filled pores is achieved at maximum dilution of phosphoric acid at high current operation states) for maximum fragment tilts here.

We interpret all of the found structural changes (the periodical structures and the electrode fragment movements) as a symptom or cause of MEA degradation but their impact on the total active catalyst surface is not yet clear. One cannot exclude that fragments can be detached or destroyed by the forces occurring during cell operation and, therewith, modify the electrical and transport properties of the electrodes [37].

5. Conclusions

We present the first synchrotron X-ray radiographic in situ study on high-temperature polymer electrolyte fuel cells (HT-PEFCs) in the through-plane viewing direction. A cell that had been subjected to a break-in procedure and a freshly assembled one were analyzed at different flow rates and current densities. The analysis reveals new details about dynamic effects in HT-PEFCs, especially about the redistribution of phosphoric acid inside the membrane electrode assembly (MEA).

However, upon increasing current density changes in the local transmittance were observed in the MEA which are assumed to be caused by non-uniform doping of the electrodes with phosphoric acid. The typical widths of regions of altered transmittance were about 1 mm. Within channel areas local transmittance variations were more pronounced as compared to rib areas. The origin of transmittance changes was largely attributed to a redistribution of phosphoric acid inside the MEA. Due to the hygroscopic nature phosphoric acid attracts (product) water. While the phosphoric acid is diluted its mass density decreases and the higher molecule mobility can facilitate local acid redistributions. The effect is more pronounced under the channels because of the lower local compression rate of the MEA which permits a stronger membrane deformation. Transmittance changes increase with increasing current densities and depend only slightly on the applied stoichiometry. All observed effects were less pronounced when no break-in procedure was applied to the cell.

The redistribution of phosphoric acid yields variations of the fragmented structure of the electrodes. The strength of the tilt of electrode fragments was found to be in accordance with the expansion and the contraction of the MEA. The comparison of radiographs taken during OCV condition before and after an operation sequence of increasing load conditions revealed irreversible modifications of the fragment structure of the catalyst layers.

Fig. 11. a) Sketch of geometrical correlations for a tilted fragment. b) Correlation of tilt displacement a and lift (height) z of the fragment edge for typical fragment dimensions $L_{frag} \approx 50-500$ μm. The light gray areas mark actual combinations of fragment dimension L_{frag} and tilt displacement a as found in the radiographs. The dark gray area schematically highlights the most frequently occurring combinations.

References

[1] C.-Y. Wang, in: W. Vielstich, A. Lamm, H.A. Gasteiger (Eds.), Handbook of Fuel Cells − Fundamentals, Technology and Applications, vol. 3, John Wiley & Sons, Chichester, 2003, pp. 337−347.
[2] C.-Y. Wang, Chemical Reviews 104 (10) (2004) 4727−4766.
[3] C. Hartnig, I. Manke, R. Kuhn, N. Kardjilov, J. Banhart, W. Lehnert, Applied Physics Letters 92 (2008) 134106.

[4] I. Manke, C. Hartnig, M. Grünerbel, W. Lehnert, N. Kardjilov, A. Haibel, A. Hilger, J. Banhart, H. Riesemeier, Applied Physics Letters 90 (2007) 174105–174111.

[5] A. Schröder, K. Wippermannn, W. Lehnert, D. Stolten, T. Sanders, T. Baumhöfer, N. Kardjilovc, Á. Hilger, J. Banhart, I. Manke, Journal of Power Sources 195 (15) (2010) 4765–4771.

[6] T. Sasabe, P. Deevanhxay, S. Tsushima, S. Hirai, Electrochemistry Communications 13 (6) (2011) 638–641.

[7] T. Sasabe, S. Tsushima, S. Hirai, International Journal of Hydrogen Energy 35 (20) (2010) 11119–11128.

[8] A. Higier, H. Liu, Journal of Power Sources 193 (2) (2009) 639–648.

[9] F. Aya, E.A. Ataa, H. Dohleb, T. Şenerc, H. Gorgun, Journal of Power Sources 167 (2) (2007) 391–397.

[10] T. Arlt, I. Manke, K. Wippermann, C. Tötzke, H. Markötter, H. Riesemeier, J. Mergel, J. Banhart, Electrochemistry Communications 13 (8) (2011) 826–829.

[11] H. Markötter, I. Manke, P. Krüger, T. Arlt, J. Haussmann, M. Klages, H. Riesemeier, C. Hartnig, J. Scholta, J. Banhart, Electrochemistry Communications 13 (9) (2011) 1001–1004.

[12] A. Pfrang, D. Veyret, G.J.M. Janssen, G. Tsotridis, Journal of Power Sources 196 (12) (2011) 5272–5276.

[13] H.-Y. Tang, A. Santamaria, J. Kurniawan, J.W. Park, T.-H. Yang, Y.-J. Sohn, Journal of Power Sources 195 (19) (2010) 6774–6781.

[14] J.P. Owejan, T.A. Trabold, D.L. Jacobson, D.R. Baker, D.S. Hussey, M. Arif, International Journal of Heat and Mass Transfer 49 (25–26) (2006) 4721–4731.

[15] A. Schröder, K. Wippermann, J. Mergel, W. Lehnert, D. Stolten, T. Sanders, T. Baumhöfer, D.U. Sauer, I. Manke, N. Kardjilov, A. Hilger, J. Schloesser, J. Banhart, C. Hartnig, Electrochemistry Communications 11 (8) (2009) 1606–1609.

[16] P. Krüger, H. Markötter, J. Haußmann, M. Klages, T. Arlt, J. Banhart, C. Hartnig, I. Manke, J. Scholta, Journal of Power Sources 196 (12) (2011) 5250–5255.

[17] J.J. Gagliardo, J.P. Owejan, T.A. Trabold, T.W. Tighe, Nuclear Instruments and Methods in Physics Research Section A: Accelerators, Spectrometers, Detectors and Associated Equipment 605 (1–2) (2009) 115–118.

[18] I. Manke, H. Markoetter, C. Totzke, N. Kardjilov, R. Grothausmann, M. Dawson, C. Hartnig, S. Haas, D. Thomas, A. Hoell, C. Genzel, J. Banhart, Advanced Engineering Materials 13 (8) (2011) 712–729.

[19] N. Kardjilov, I. Manke, A. Hilger, M. Strobl, J. Banhart, Materials Today 14 (6) (2011) 248–256.

[20] W. Maier, T. Arlt, C. Wannek, I. Manke, H. Riesemeier, P. Krüger, J. Scholta, W. Lehnert, J. Banhart, D. Stolten, Electrochemistry Communications 12 (10) (2010) 1436–1438.

[21] R. Kuhn, J. Scholta, P. Krüger, C. Hartnig, W. Lehnert, T. Arlt, I. Manke, Journal of Power Sources 196 (12) (2010) 5231–5239.

[22] W. Maier, T. Arlt, K. Wippermann, C. Wannek, I. Manke, W. Lehnert, D. Stolten, Journal of the Electrochemical Society 159 (8) (2012) F398–F404.

[23] J. Banhart, A. Borbely, K. Dzieciol, F. Garcia-Moreno, I. Manke, N. Kardjilov, A.R. Kaysser-Pyzalla, M. Strobl, W. Treimer, International Journal of Materials Research 101 (9) (2010) 1069–1079.

[24] J. Banhart (Ed.), Advanced Tomographic Methods in Materials Research and Engineering, Oxford University Press, Oxford, 2008.

[25] T. Arlt, I. Manke, K. Wippermann, H. Riesemeier, J. Mergel, J. Banhart, Journal of Power Sources 221 (2013) 210–216.

[26] G. Giacoppo, O. Barbera. A. Carbone, I. Gatto, A. Saccà, R. Pedicini , E. Passalacqua , International Journal of Hydrogen Energy, Available online 11 May 2013, ISSN 0360-3199, http://dx.doi.org/10.1016/j.ijhydene.2013.04.044.

[27] S. Galbiati, A. Baricci, A. Casalegno, R. Marchesi, International Journal of Hydrogen Energy 37 (3) (2012) 2462–2469.

[28] C.J.T. de Grotthuss, Annali de Chimica 58 (1806) 54–73.

[29] R. He, Q. Li, G. Xiao, N.J. Bjerrum, Journal of Membrane Science 226 (2003) 169–184.

[30] R.F. Jameson, Journal of the Chemical Society (1959) 752.

[31] D.-T. Chin, H. Chang, Journal of Applied Electrochemistry 19 (1989) 95.

[32] W. Görner, M.P. Hentschel, B.R. Müller, H. Riesemeier, M. Krumrey, G. Ulm, W. Diete, U. Klein, R. Frahm, Nuclear Instruments and Methods in Physics Research Section A: Accelerators, Spectrometers, Detectors and Associated Equipment 467–468 (2001) 703–706.

[33] http://www.helmholtz-berlin.de/user/experimental-infrastructures/instruments-photons/bessy-beamline_en.html, Feb 06, 2013.

[34] Data Sheet pco, http://www.pco.de/sensitive-cameras/pco4000/, Feb 06, 2013.

[35] C. Wannek, W. Lehnert, J. Mergel, Journal of Power Sources 192 (2009) 258.

[36] D.-T. Chin, H.H. Chang, Journal of Applied Electrochemistry 19 (1989) 95–99.

[37] H. Schulenburg, B. Schwanitz, N. Linse, G.G. Scherer, A. Wokaun, J. Krbanjevic, R. Grothausmann, I. Manke, Journal of Physical Chemistry C 115 (29) (2011) 14236–14243.